Magnetic anisotropy of Co_xPt_{1-x} clusters embedded in matrix: Influences of the cluster chemical composition and the matrix nature

S. Rohart,[1,*] C. Raufast,[1] L. Favre,[1,†] E. Bernstein,[1] E. Bonet,[2] and V. Dupuis[1]

[1]*Laboratoire de Physique de la Matière Condensée et Nanostructures, Université Lyon 1; CNRS, UMR 5586, Domaine Scientifique de la Doua, F-69622 Villeurbanne Cedex; France*

[2]*Laboratoire Louis Néel; CNRS, UPR 5051, BP 166, F-38042 Grenoble Cedex 9; France*

(Dated: May 4, 2006)

Abstract

We report on the magnetic properties of Co_xPt_{1-x} clusters embedded in various matrices. Using a careful analysis of magnetization curves and ZFC susceptibility measurements, we determine the clusters magnetic anisotropy energy (MAE) and separate the surface and volume contributions. By comparing different chemical compositions, we show that a small amount of Pt (15 %) induces an important increase in the volume anisotropy with respect to pure Co clusters, even in chemically disordered fcc clusters. Comparing the measurements of clusters embedded in Nb and MgO matrices, we show that the oxide matrix induces an important increase of the surface MAE attributed to the formation of an antiferromagnetic CoO shell around the clusters.

PACS numbers: 61.46.Bc, 75.30.Gw, 75.75.+a

ccsd-00023734, version 2 - 4 May 2006

I. INTRODUCTION

Nanometer-sized magnetic particles have been attracting an increasing interest over the last decades as their properties considerably differ from those of bulk materials due to the non negligible fraction of atoms located at the surfaces or the interfaces. Enhancement of the orbital magnetic moment as well as the magnetic anisotropy energy (MAE) at the less coordinated atoms were observed on many system, from single atoms,[1] free,[2,3,4] supported[5,6,7] and embedded clusters.[8,9] From a technological point of view, such nanostructures are potential candidates to increase the storage media density.[10] However, applications are limited by superparamagnetism: due to their reduced sizes, the nanoparticles MAE is not sufficient to stabilize the magnetization direction, which fluctuates due to thermal activation. Then, the need for nanomagnets with higher thermal stability drives the need for high MAE nanomaterials.

In very small nanostructures, where surface to volume atom number ratio is not negligible, two contributions to the MAE are found originating from volume and surface or interface.[8,11] The volume anisotropy is mainly due to the clusters crystallographic structure, via the magnetocrystalline anisotropy (MCA). As atomic stacking with a high symmetry (like cubic staking) does not favor a high MCA, intense efforts are devoted to the production of mixed clusters made of a magnetic material (Co, Fe, Ni) with a $4d$ or $5d$ transition metal (Pd, Pt).[9,12,13] When ordered in the $L1_0$ tetragonal phase, such mixed bi-metallic systems show very strong MCA.[14,15,16] The surface anisotropy has two origins. On the one hand, as the lower coordinated atoms at the surface are in a less symmetric environment, they present an enhanced MAE as compared to the bulk.[1,8,11] On the other hand, the contact with a non ferromagnetic matrix induces an interfacial anisotropy, whose origin depends on the matrix nature. In the case of metallic matrices, the interfacial anisotropy is due to the spin-orbit coupling and hybridization between cluster and matrix atom orbitals, as shown in Co/Pt multilayers[17] and Co clusters embedded in Pt.[18] In the case of antiferromagnetic matrices, the interfacial anisotropy is due to the exchange bias phenomenon[19] as shown for Co cluster embedded in CoO.[20]

In this study, we present magnetic measurements on mixed Co_xPt_{1-x} clusters (with x ranging from 0 to 1) embedded in two different matrices: a metallic one (Nb) and an oxide one (MgO). With a careful analysis of hysteresis loops and Zero Field Cooled (ZFC) sus-

ceptibility measurements, we separate the volume and surface magnetic anisotropy energies. We then show that, even in non chemically ordered fcc clusters, the addition of platinum increases the volume anisotropy with respect to pure Co. We also show that a high surface anisotropy is found when clusters are embedded in the oxide matrix, due to the formation of a CoO shell around the clusters.

II. SAMPLE ELABORATION AND CHARACTERIZATION

The samples are elaborated using the co-deposition of preformed clusters in the gas phase and of an atomic flux for the matrix.[21,22] The clusters are produced by the condensation of a plasma obtained by laser vaporization on a metallic rod.[23] We use a Nd:YAG laser ($\lambda =$ 532 nm, pulse duration of a few nanoseconds, frequency up to 30 Hz) to vaporize a mixed Co_xPt_{1-x} rod. A continuous He flux (about 20 mbar) is injected in the vaporization chamber to cool down the plasma. Clusters nucleate and are stabilized during a supersonic expansion at the exit nozzle of the source. It produces a cluster beam of about 10^{-3} cluster/nm^2/s. Clusters are deposited in the low energy cluster beam deposition (LECBD) regime[22] in a UHV chamber (base pressure 5×10^{-10} mbar) on a Si(001) substrate. Due to their low kinetic energy, clusters do not fragment upon impact and conserve their morphology when they are deposited.[22] The matrix is evaporated using an electron gun evaporator. Nb is evaporated at 0.2 nm/s and MgO is evaporated at 0.02 nm/s. The pressure during the co-deposition is below 5×10^{-8} mbar and falls down rapidly after the process.

We have produced four types of clusters, using four target rods with different compositions (cf. table I). Using energy dispersive x-rays (EDX) and Rutherford back scattering (RBS) spectroscopy measurements, we have characterized the clusters composition. Our production technique produces mixed clusters with roughly the same composition as the target.[24,25,26,27] As shown in table I, the general tendency is to produce Co-enriched clusters. This phenomenon may be due to a predominance of Co atoms evaporation upon laser impact or a re-evaporation of Pt atoms during the expansion. Then the studied clusters have the following compositions: Co, $Co_{85}Pt_{15}$, $Co_{58}Pt_{42}$, $Co_{30}Pt_{70}$ (the indices indicate the element proportion en percent). The morphology, crystallography and size distribution of the clusters have been determined by transmission electron microscopy (TEM) experiments, performed on clusters deposited on microscopy grids coated by an amorphous carbon film.

A typical image and diameter distribution is shown in figure 1 for the $Co_{85}Pt_{15}$ clusters. In each case, the diameters follow a Log-normal distribution. The mean diameter is slightly higher for pure Co clusters (3.2 nm) than for the mixed clusters (about 2 nm - see table I). The crystallography was determined by the electron diffraction patterns and high resolution TEM images (HRTEM). In the case of the pure Co clusters, the HRTEM images show a {111} interreticular distance of about (2.04±0.02) Å, indicating a fcc crystalline structure. In the case of the mixed clusters, the diffraction patterns show a {111} interreticular distance, which lies between the Co fcc (2.05 Å) and Pt fcc (2.27 Å) {111} interreticular distances, typical of disordered alloys. The fcc structure is further confirmed by the HRTEM images, which show that clusters have a faceted truncated octahedron morphology,[8,28] corresponding to the typical equilibrium shape of fcc nanocystallites.[29]

TABLE I: Isolated clusters morphological characteristics depending on the target rod. D_m corresponds to the median diameter and σ to the dispersion. The composition is determined using EDX spectroscopy. The values are in good agreement (less than 3 % error) with RBS measurement.

Target rod	Cluster	D_m	σ
Co	Co	3.2 nm	0.25
Co_3Pt	$Co_{85}Pt_{15}$	2.0 nm	0.35
CoPt	$Co_{58}Pt_{42}$	1.95 nm	0.35
$CoPt_3$	$Co_{30}Pt_{70}$	1.9 nm	0.3

In a second step, we have considered the clusters embedded in the matrices. We have used several characterization x-rays based techniques.[28,30] These measurements have shown that, from the crystallographic point of view, the interface is not sharp. From extended x-rays absorption fine structures (EXAFS) measurement and simulations on Co clusters embedded in a Nb matrix,[30] we show that an intermixing occurs on the two first layers leading to a CoNb shell, reducing the pure Co cluster diameter. From grazing incidence x-rays small and wide angle scattering (GISAXS and GIWAXS) on $Co_{58}Pt_{42}$ clusters embedded in a MgO matrix,[28] the occurrence of the set of Bragg peaks confirms the presence of only one alloyed phase with a {111} interreticular distance of 2.21 Å but with a mean CoPt nanocrystallite diameter of 1.3 nm. This result is due to the oxidation of the cluster surface, which has been shown by x-ray absorption spectroscopy at the $L_{2,3}$ Co edges. Then, the clusters have

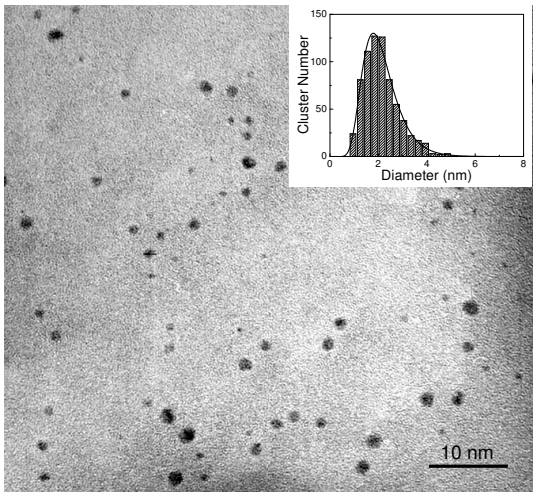


FIG. 1: TEM micrograph of the $Co_{85}Pt_{15}$ clusters deposited on an amorphous carbon grid. Inset: diameter distribution. The histogram corresponds to the TEM measurements and the continuous line corresponds to a Log-normal fit.

a CoPt core and a Co(Pt)O shell. From such a diffuse cluster surface, one could expect inhomogeneous magnetic properties. Surprisingly, it was already shown from microSQUID measurements performed on single Co clusters embedded in a Nb matrix that even if the CoNb shell is not magnetic, the Co core conserves the magnetic properties of a well defined faceted cluster.[8,11,30] In the following we show that the magnetic properties of our clusters are also quite homogeneous.

III. MAGNETIC MEASUREMENTS AND QUANTITATIVE ANALYSIS

The magnetic measurements have been performed using a superconducting quantum interference device (SQUID) at various temperatures (except for the Co:Nb sample, which was measured using a vibrating sample magnetometer.[30]) In order to extract the single isolated cluster magnetic behavior and avoid any cluster magnetic interactions, we have studied low concentrated samples. For the clusters embedded in the Nb matrix the concentration was about 0.1 % in volume and for the clusters embedded in the MgO matrix, the concentration was about 5 % in volume. At these concentrations the mean distance between clusters is about 15 nm in Nb and 5 nm in MgO. This is sufficiently large to discard Ruderman-Kittel-Kasuya-Yasuda interactions in metallic matrices, which vanish above a few nanometers.[31,32]

Dipolar interactions can also be neglected as the typical interaction temperature[33] is much lower than our measurement temperatures (respectively 0.2 K in Nb and 4 K in MgO). We have measured the four cluster types in both matrices. In the following, samples are referred as C:M with C=Co, $Co_{85}Pt_{15}$, $Co_{58}Pt_{42}$ or $Co_{30}Pt_{70}$ the cluster type and M=Nb or MgO the matrix.

A. Experimental results

The $M(H)$ curves were recorded at various temperatures, from 2 K to 300 K, and for $\mu_0 H = -5$ to $+5$ T (field sweeping rate 1 mT/s). Except for the $Co_{30}Pt_{70}$ clusters, we have always observed a clear ferromagnetic signal at low temperature. The weak signal for the $Co_{30}Pt_{70}$ clusters may be due to a too low ordering temperature, as it is well known that the Co_xPt_{1-x} bulk Curie temperature decreases with increasing the Pt proportion.[34] Therefore, we only present in the following the results for the Co, $Co_{85}Pt_{15}$ and $Co_{58}Pt_{42}$ clusters.

At high temperature, the $M(H)$ curves are not hysteretic on any sample, typical of a superparamagnetic (SPM) behavior as will be discussed later. On the contrary, the curves taken at low temperature show open hysteresis loops, typical of a ferromagnetic or blocked regime (FM). Due to the superconducting transition in Nb below 8 K, background subtraction becomes hazardous for the samples with the Nb matrix. Therefore we cannot compare the data taken at the lowest temperatures and we focus on the curves measured at 10 K (fig. 2). The transition between SPM and FM regimes was characterized using the so-called zero field cooled-field cooled (ZFC-FC) protocol (fig. 3), recorded in a 5 to 10 mT field, with a temperature sweeping rate of few tens of mK/s. For every measurement, the ZFC curve shows a maximum at $T = T_{\max}$, which is related to the blocking temperature T_B of the particles. For $T > T_{\max}$, we observe a decrease of M, which is proportional to T^{-1}, typical of SPM.

As a general trend, we observe that the peak temperature $T_{\max}$ in the ZFC curves for a given type of cluster is systematically higher for clusters embedded in MgO than for clusters embedded in Nb. In the same way, the coercive fields H_C and remanent to saturation magnetization ratios M_R/M_S are also systematically higher for clusters embedded in MgO than for clusters embedded in Nb. This shows that the MgO matrix induces higher magnetic anisotropy energy than the Nb matrix. However, the origin of this result is difficult to discuss

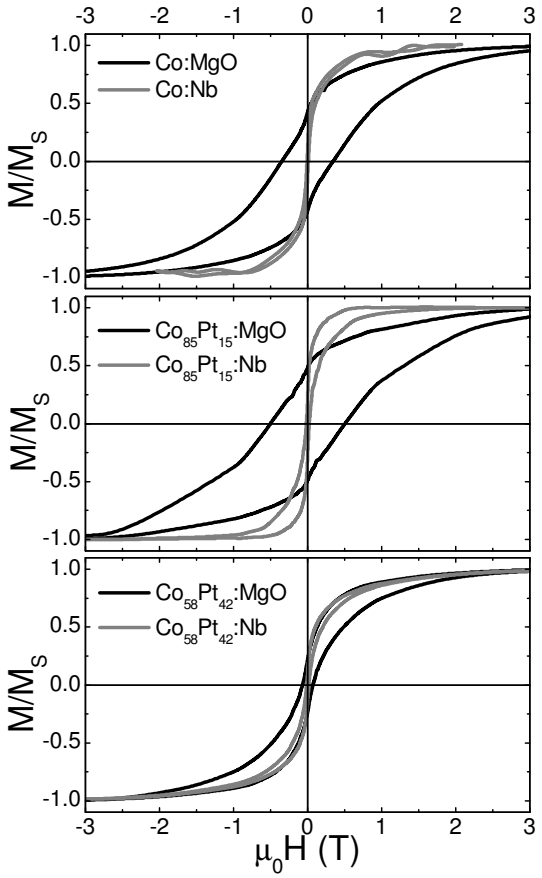


FIG. 2: Normalized hysteresis loops measured at $T = 10$ K on the samples with Co, $Co_{85}Pt_{15}$ and $Co_{58}Pt_{42}$ clusters. The dark lines correspond to the measurements in the MgO matrix and the grey lines correspond to the measurements in the Nb matrix.

as the clusters do not have the same magnetic size in both matrices due to the intermixing at the interface. In the following, we present our analysis of the measurements and show a model to fit the ZFC-FC curves. This analysis enables us to deduce quantitatively the surface and volume anisotropies, which are independent of the cluster magnetic volume.

B. Magnetic size

The first point of the analysis is to determine precisely the clusters magnetic volume and its corresponding distribution in the samples. For that purpose, we focus on the superparamagnetic $M(H)$ curves measured at high temperatures ($T \gg T_{\max}$). At these temperatures, the thermal energy is high compared to the MAE, which can be neglected.[35] The magnetic behavior can be described by the classical Langevin function. In order to fit the measure-

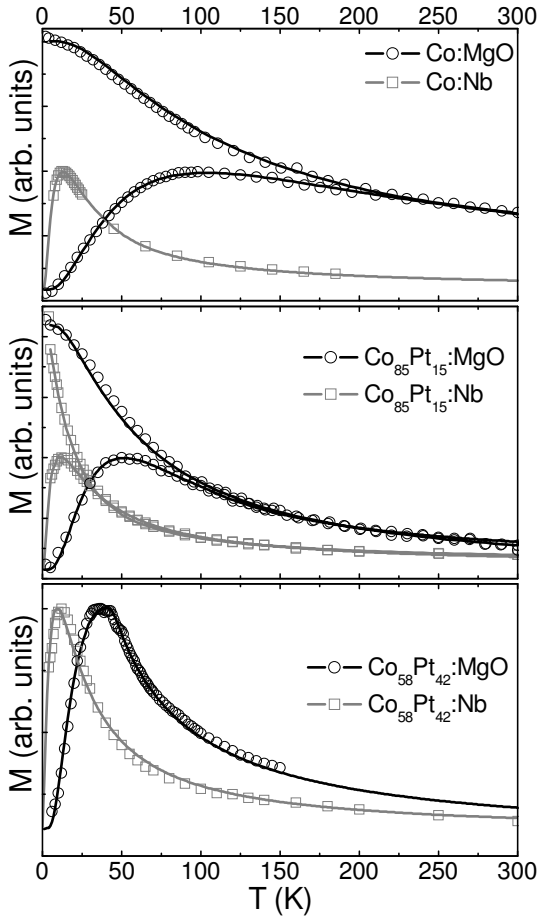


FIG. 3: ZFC-FC curves measured on the Co, $Co_{85}Pt_{15}$ and $Co_{58}Pt_{42}$ clusters embedded in MgO and Nb matrices. The curves were recorded in a small field of 5 mT (Co:MgO and $Co_{85}Pt_{15}$:MgO) or 10 mT (Co:Nb, $Co_{85}Pt_{15}$:Nb, $Co_{58}Pt_{42}$:Nb and $Co_{58}Pt_{42}$:MgO). The dots correspond to the measurements and the continuous lines correspond to the fits using the model described below.

ments, we take into account the magnetic volume distribution. Then, the measurements are described by the convolution of a Langevin function with the magnetic volume distribution as explained in Ref. 30. Following the TEM results, we assume a Log-normal distribution for the cluster magnetic diameter. As magnetization enhancement only occurs for clusters containing less than about 500 atoms (about 2 nm in diameter),[3] we use bulk magnetization values. In pure Co clusters, we take $m_{Co} = 1.7\ \mu_B$.[30] In Co_xPt_{1-x} clusters we take $m_{Co} = 1.9\ \mu_B$ and $m_{Pt} = 0.45\ \mu_B$.[36] For each sample, we fit at least two measurements, for $T > 2T_{\max}$. An example for the Co:MgO sample is shown in fig. 4 and the results are shown in table II.

We systematically find a reduced magnetic size as compared to the TEM measured size

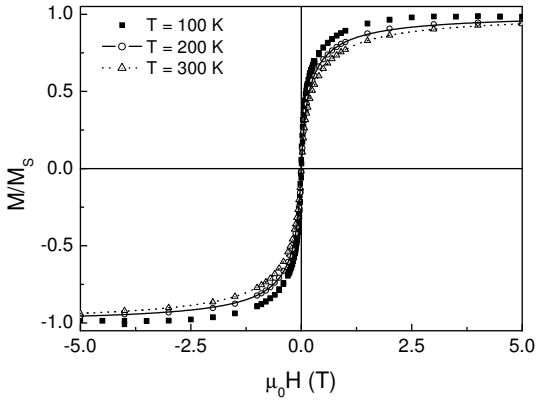


FIG. 4: Superparamagnetic $M(H)$ curves measured on the Co:MgO sample at 100 K, 200 K and 300 K. The two measures at the highest temperatures are fitted using the convolution of a Langevin function with Log-normal distribution of the magnetic diameter. The curve recorded at 100 K cannot be fitted with the same parameters due to a non negligible MAE.

(table I). This is due to the cluster-matrix interface, which induces some dead surface layers. In the case of the clusters embedded in the Nb matrix, the mean diameter is reduced by about 1 nm, which corresponds to two dead surface layers. This is coherent with a previous EXAFS study on the Co:Nb sample,[30] which has shown the formation of a non magnetic CoNb alloy for the first two surface layers. X-ray magnetic circular dichroism (XMCD) measurements on the Co:Nb[37] and $Co_{58}Pt_{42}$:Nb samples[28] have also shown the same results. The mean spin moments μ_S determined from XMCD sum rules are found to be lower than the bulk spin moment. The ratio (respectively $\mu_S/\mu_{S,bulk} = 0.33$ for Co:Nb and 0.12 for $Co_{58}Pt_{42}$:Nb) is close to the ratio of the magnetic volume to the cluster volume (respectively 0.37 for Co:Nb and 0.16 for $Co_{58}Pt_{42}$:Nb), which corroborates our magnetic volume determination. In the case of the clusters embedded in the MgO matrix, the mean diameter is reduced by about 0.5 nm for $Co_{85}Pt_{15}$:MgO and $Co_{58}Pt_{42}$:MgO and 1 nm for Co:MgO, which corresponds respectively to one and two dead surface layers. In the case of $Co_{58}Pt_{42}$:MgO, this is coherent with the x-ray diffraction measurements and with the XMCD.[28] In this last case, the mean spin moment to bulk spin moment ratio was found to be 0.34, close to the magnetic volume to cluster volume ratio (0.41). In this case, the dead layers are due to the formation of a Co(Pt)O antiferromagnetic shell around the cluster magnetic core, observed in the Co L_3 multiplet peak in the x-ray absorption peak.

TABLE II: Magnetic characteristics of the samples deduced from the magnetic measurements and their modeling. The magnetic median diameter $D_{m,\mathrm{Mag}}$ and dispersion σ_{Mag} are obtained from the Langevin fit of the superparamagnetic M(H) curves. $T_{\max}$ corresponds to the maximum ZFC susceptibility temperature. H_C is the coercive field at 10 K. The remanent to saturation magnetization ratio is measured at 10 K. The values in parenthesis correspond to the theoretical value calculated from the model described below. K_V and K_S are determined by fitting the ZFC-FC curves using the same model.

Sample	$D_{m,\mathrm{Mag}}$	σ_{Mag}	$T_{\max}$	$\mu_0 H_C$	M_R/M_S	K_V	K_S
Co:MgO	2.30 nm	0.40	100 K	340 mT	0.43 (0.49)	(40 ± 21) kJ/m^3	(360 ± 10) μJ/m^2
Co:Nb	2.27 nm	0.39	12 K	5 mT	0.10 (0.15)	(60 ± 15) kJ/m^3	(45 ± 5) μJ/m^2
$Co_{85}Pt_{15}$:MgO	1.45 nm	0.38	50 K	500 mT	0.49 (0.47)	(200 ± 19) kJ/m^3	(420 ± 11) μJ/m^2
$Co_{85}Pt_{15}$:Nb	1.00 nm	0.40	13 K	20 mT	0.25 (0.21)	(170 ± 13) kJ/m^3	(160 ± 13) μJ/m^2
$Co_{58}Pt_{42}$:MgO	1.52 nm	0.38	39 K	70 mT	0.23 (0.27)	(100 ± 18) kJ/m^3	(200 ± 15) μJ/m^2
$Co_{58}Pt_{42}$:Nb	0.97 nm	0.41	12 K	15 mT	0.13 (0.13)	(110 ± 14) kJ/m^3	(170 ± 12) μJ/m^2

C. Surface and volume anisotropies

We now determine the magnetic anisotropy energies in the samples. For this purpose we focus on the ZFC-FC measurements. In many studies, the MAE is evaluated by considering that $T_{\max}$ is the clusters blocking temperature. Whereas this is true for a monodisperse cluster assembly, such an assumption leads to an overestimation of the MAE for a distributed assembly. In the following we expose a model which describes the ZFC-FC curves for a monodisperse cluster assembly. Then we fit the measurements, using a convolution of the monodisperse assembly model with the magnetic volume distribution determined previously.

We consider that our clusters are single domain magnets with a uniaxial magnetic anisotropy, a quite common assumption for such nanostructures.[8,38] As no crystalline direction or orientation is favored during the LECBD and because the matrix is polycrystalline, the cluster anisotropy axes are randomly oriented. The cluster magnetic energy is described by the Stoner-Wohlfarth Hamiltonian.[39] They can be magnetized in two directions (named

1 and 2 in the following), which depend on the anisotropy axis orientation and external field. The transition from SPM to FM regimes is due to kinetic and thermal effects. Therefore, the relaxation of the magnetic moments is described using the rate equation[40,41,42]

$$\frac{dn_1}{dt} = -\nu_{12} n_1 + \nu_{21}(1 - n_1), \tag{1}$$

where n_1 is the proportion of clusters, whose magnetization points in the direction 1 and ν_{12} (resp. ν_{21}) is the switching rate from direction 1 to 2 (resp. from 2 to 1). The switching rates are expressed as $\nu_i = \nu_0 \exp(-\Delta E_i / k_B T)$ (with $i = 12$ or 21) where ΔE_i is the energy barrier and ν_0 the attempt frequency (about 10^{10} Hz).[38] These energy barriers depend on the external magnetic field H and its orientation with respect to the cluster anisotropy axis. Unfortunately, no analytical expression can be found for the energy barriers if the external magnetic field H is not aligned with the anisotropy axis. However, in the case of a low field ($\mu_0 H \ll K/\mu$, with K the cluster MAE and μ the cluster magnetic moment), it can be estimated as[42]

$$\Delta E_{12} = K\left[1 - 2\frac{H}{H_K}(\sin\psi - \cos\psi)\right] \tag{2a}$$

$$\Delta E_{21} = K\left[1 - 2\frac{H}{H_K}(\sin\psi + \cos\psi)\right], \tag{2b}$$

where $\mu_0 H_K = 2K/\mu$ is the anisotropy field and ψ is the angle between the magnetic field and the anisotropy axis. For an assembly of clusters with random orientation of the easy axis, the magnetization along the field direction M is the average of all the possible orientations. If we further assume $\mu_0 H \ll k_B T/\mu$ and H constant, then the magnetization M is the solution of

$$\tau(T)\frac{dM}{dt} + M = \frac{\mu_0 \mu^2 H \eta}{3K}\left(1 + \frac{K}{k_B T}\right), \tag{3}$$

with η the cluster density and $\tau(T) = \frac{1}{2\nu_0}\exp(K/k_B T)$, the relaxation time. In the ZFC-FC measurement protocol, the sample is previously thermally demagnetized. Then, the initial condition is $M_0 = \mu_0 \mu^2 H \eta / 3K$, which corresponds to the magnetic susceptibility due to the displacement of the energy minima by the external magnetic field.[42]

In order to find the ZFC magnetization $M_{\mathrm{ZFC}}(T)$, we hold T constant and integrate eq. (3) for a temperature T' swept from 0 to T. When T' is close to $T \ll K/k_B$, the relaxation time $\tau(T') \simeq \tau(T)\exp[(T - T')K/k_B T^2]$ varies on a temperature scale $k_B T'^2/K \ll T'$ and we can therefore keep the constant T in the right hand of eq. (3). Given a constant temperature

sweeping rate dT/dt, we have then the solution

$$M_{\mathrm{ZFC}}(T) = \frac{\mu_0 \mu^2 H \eta}{3K}\left[1 + \frac{K}{k_B T}(1 - e^{-\delta t/\tau(T)})\right], \tag{4}$$

where $\delta t = k_B T^2 (K dT/dt)^{-1}$. This is also the magnetization we would get by first stepping the temperature from 0 to T and then letting M relax for a characteristic time δt at constant T. We should notice that when $T \ll K/k_B$ is not true, the solution (4) still holds, since in this regime M_{ZFC} has always its equilibrium value.

In order to take into account the magnetic size distribution in the fitting procedure, we need to know the relation between size and MAE, which is not trivial as surface and interface effects are known to play an important role at this size range.[6,8] We then write the MAE as a combination of volume and surface anisotropies: $K = \frac{\pi}{6} D^3 K_V + \pi D^2 K_S$, where K_V and K_S are respectively the volume and surface anisotropies. In practice, we use eq. (4) to fit the experimental ZFC curves and determine K_V and K_S. Then we use a numerical integration of eq. (3), with the previously determined parameters to simulate the FC curves. The results of the modelling are shown in figure 3 and the fit parameters are reported for each sample in table II.

Equation (3) does not allow performing a calculation of the whole hysteresis loops, as it is only valid at low magnetic fields. However, it allows the determination of the remanence to saturation magnetization ratio. At $T = 0$ K, this ratio should be $\frac{1}{2}$ for an assembly of cluster with randomly oriented anisotropy axis.[30] Considering that the magnetization relaxation is non negligible for $\mu_0 \mu H < k_B T$, the measured value corresponds to the magnetization reached after the typical time $\delta t'$ in zero field:

$$\frac{M_R(T)}{M_S} = \frac{M_R(T = 0\ \mathrm{K})}{M_S} e^{-\delta t'/\tau(T)} = \frac{1}{2} e^{-\delta t'/\tau(T)}, \tag{5}$$

where $\delta t' = k_B T (\mu_0 \mu dH/dt)^{-1}$. Taking into account the volume distribution, and using the K_S and K_V values obtained previously, we have calculated $M_R/M_S(T = 10\ \mathrm{K})$ for each sample. The results shown in table II are in quite good agreement with the experimental values.

IV. DISCUSSION

The volume anisotropies found for a given cluster composition in both matrices are nearly found equal. This result justifies our separation of volume and surface anisotropies: the

volume anisotropy is only linked to the type of cluster whereas the surface anisotropy is related to the cluster surface and the matrix nature. We find that the mixed clusters have significantly higher volume anisotropy as compared to the pure Co clusters. Then, although no chemical ordering was found in the mixed clusters, the Pt atoms still favors a MAE enhancement. This result could be attributed to a finite size effect: due to the small cluster size, the atoms distribution cannot be totaly homogeneous in the cluster and a small chemical anisotropy can be observed, leading to an enhanced anisotropy, via the hybridization between Co $3d$ and Pt $5d$ orbitals. K_V is found to be maximum for the $Co_{85}Pt_{15}$ clusters (three times the Co volume anisotropy). Note that for the chemical ordered phases a higher volume anisotropy is expected for the $L1_0$ CoPt phase than for the $L1_2$ Co_3Pt one. As we observe the opposite tendency, the origin of the higher K_V in the $Co_{85}Pt_{15}$ could be due to a small chemical ordering in the cluster core. This hypothesis cannot be proved up to now but we are currently performing high resolution EDX and TEM measurements, and simulations to obtain a more precise crystallographic characterization.

Concerning the surface anisotropies, the variation according to the cluster composition is non-trivial. On the one hand, for clusters embedded in Nb, we observe that K_S increases with the proportion of Pt. On the other hand, for clusters embedded in MgO, K_S is maximum for the $Co_{85}Pt_{15}$. This complex result comes from the fact that K_S has two origins. The first one ($K_{S,\mathrm{C}}$) is intrinsic to the cluster (independent of the matrix) and is due to the low symmetry and atomic coordination at the cluster surface.[1,11] The second one ($K_{S,\mathrm{C/M}}$) is due to the cluster/matrix interface and then depends on both cluster and matrix. It was already shown that the interface anisotropy for Co clusters embedded in Nb is negligible.[8,11] Assuming that this fact is still valid for the mixed clusters, it is possible to estimate the different contributions from our measurements (see table III). From this estimation we find that the Pt atoms induce an enhancement of the cluster intrinsic surface anisotropy as compared to pure clusters. This result is attributed to the presence of Pt atoms at the surface, which decrease the coordination number of the cobalt surface atoms.

We now discuss the origin of the interface anisotropy of the clusters embedded in MgO. We note that the very high surface anisotropy found for the pure Co clusters embedded in MgO matrix is very close to the one found in a Pt matrix (K_S(Co:Pt) = 300 μJ/m^2).[18] However, the origin is completely different in the two cases. In the case of the Pt matrix, the K_S enhancement is due to the hybridization between Co and Pt atoms at the interface,

TABLE III: Intrinsic and interface anisotropy of the cluster embedded in Nb and MgO estimated from the measurements (table II) as $K_S(\mathrm{C:M}) = K_{S,\mathrm{C}} + K_{S,\mathrm{C/M}}$. The interface anisotropy of cluster embedded in Nb is supposed to be zero.

Cluster	$K_{S,\mathrm{C}}$	$K_{S,\mathrm{C/Nb}}$	$K_{S,\mathrm{C/MgO}}$
Co	45 μJ/m^2	0	315 μJ/m^2
$Co_{85}Pt_{15}$	160 μJ/m^2	0	260 μJ/m^2
$Co_{58}Pt_{42}$	170 μJ/m^2	0	30 μJ/m^2

a well known effect in the Co/Pt multilayers.[17,43] Such an effect is not possible in the case of the MgO matrix. The origin is rather due to the formation of an oxide shell around the clusters, as it was observed in the x-ray absorption spectra.[28] It is well known that the interface between an antiferromagnetic (AFM) and a ferromagnetic layer leads to the so-called exchange anisotropy and to the exchange bias phenomenon.[19] Concerning nanoparticles, this effect was shown to induce an important increase of the anisotropy.[20,44] In order to evidence the exchange bias phenomena, we have measured the low temperature hysteresis loops after a field cooled under a high magnetic field. After a 3 T field cooled, the $Co_{58}Pt_{42}$:MgO sample has shown a small 12 ± 5 mT exchange bias field at 6 K. After a 6 T field cooled, the Co:MgO sample has shown no exchange bias at 2 K. This unclear exchange bias observation may be related to the small thickness of the CoO shell. Indeed, in such a case, the AFM shell MAE is too low as compared to the coupling energy between the FM core and AFM shell. Then the magnetic moments in the shell rotate coherently with the FM core[45] and the energy to overcome in order to reverse the cluster magnetization corresponds to the sum of the core and shell MAE. Concerning the cluster/MgO interface anisotropy variation with the cluster chemical composition, we remark that it decreases when the Pt proportion is increased and we find that this contribution is weak for the $Co_{58}Pt_{42}$ clusters. We attribute this result to the presence of Pt atoms at the cluster surface, which decrease the quality of the antiferromagnetic ordering in the oxide shell, as it was already observed in ferromagnetic/antiferromagnetic multilayers.[46]

V. CONCLUSION

In conclusion, we have studied the magnetic anisotropy of well defined Co_xPt_{1-x} nanoclusters embedded in Nb and MgO matrices. Using a careful analysis of $M(H)$ curves and ZFC-FC susceptibility measurements, we have determined the magnetic anisotropy of the clusters and separated the surface and volume contributions. By comparing samples of different compositions, we have shown that a small amount of Pt (15 %) in the clusters is responsible for a strong increase of the volume anisotropy, even if the clusters are fcc chemically disordered. Once more, we have shown that the MgO matrix induces an enhanced surface anisotropy due to the partial oxidation of the surface of the clusters.

Acknowledgments

The authors are indebted to O. Boisron, G. Guiraud and C. Clavier for their continuous technical assistance and developments during LECBD experiments and to E. Eyraud for his technical assistance during the SQUID measurements. We acknowledge support from the European Community (STREP SFINx no. NMP2-CT-2003-505587).

---

* Electronic address: srohart@lpmcn.univ-lyon1.fr

† Current address: L2MP, Université Aix-Marseille III; CNRS UMR 6137, F-13397 Marseille Cedex 20; France

[1] P. Gambardella, S. Rusponi, M. Veronese, S. S. Dehsi, C. Grazioli, A. Dallmeyer, I. Cabria, R. Zeller, P. H. Dederichs, K. Kern, et al., Science **300**, 1130 (2003).

[2] J. P. Bucher, D. C. Douglass, and L. A. Bloomfield, Phys. Rev. Lett. **66**, 3052 (1991).

[3] I. M. Billas, A. Châtelin, and W. A. de Heer, Science **265**, 1682 (1994).

[4] Y. Xie and J. A. Blackman, J. Phys.: Condens. Matter **15**, L615 (2003).

[5] H. A. Dürr, S. S. Dhesi, E. Dudzik, D. Knabben, G. van der Laan, J. B. Goedkoop, and F. U. Hillebrecht, Phys. Rev. B **59**, R701 (1999).

[6] S. Rusponi, T. Cren, N. Weiss, M. Epple, P. Buluschek, L. Claude, and H. Brune, Nature Mater. **2**, 546 (203).

[7] N. Weiss, T. Cren, M. Epple, S. Rusponi, G. Baudot, S. Rohart, A. Tejeda, V. Repain, S. Rousset, P. Ohresser, et al., Phys. Rev. Lett. **95**, 157204 (2005).

[8] M. Jamet, W. Wernsdorfer, C. Thirion, D. Mailly, V. Dupuis, P. Mélinon, and A. Pérez, Phys. Rev. Lett. **86**, 4676 (2001).

[9] J. Bansmann, S. H. Baker, C. Binns, J. A. Blackman, J. P. Bucher, J. Dorantes-Dávila, V. Dupuis, L. Favre, D. Kechrakos, A. Kleibert, et al., Surf. Sci. Rep. **56**, 189 (2004).

[10] M. L. Plumer, J. van Ek, and D. Weller, *The physics of ultra-high-density magnetic recording* (Springer, Berlin, 2001).

[11] M. Jamet, W. Wernsdorfer, C. Thirion, V. Dupuis, P. Mélinon, A. Pérez, and D. Mailly, Phys. Rev. B **69**, 024401 (2004).

[12] G. M. Pastor, J. Dorantes-Dávila, S. Pick, and H. Dreyssé, Phys. Rev. Lett. **75**, 326 (1995).

[13] L. Szunyogh, P. Weinberger, and C. Sommers, Phys. Rev. B **60**, 11910 (1999).

[14] S. Sun, C. B. Murray, D. Weller, L. Folks, and A. Moser, Science **287**, 1989 (2000).

[15] M. Chen and D. Nikles, J. Appl. Phys. **91**, 8477 (2002).

[16] C. Petit, S. Rusponi, and H. Brune, J. Appl. Phys. **95**, 4251 (2004).

[17] N. Nakajima, T. Koide, T. Shidara, H. Miyauchi, H. Fukutani, A. Fujimori, K. Iio, T. Katayama, M. Nývlt, and Y. Suzuki, Phys. Rev. Lett. **81**, 5229 (1998).

[18] M. Jamet, M. Négrier, V. Dupuis, J. Tuaillon-Combes, P. Mélinon, A. Pérez, W. Wernsdorfer, B. Barbara, and B. Baguenard, J. Magn. Magn. Matters **237**, 293 (2001).

[19] W. H. Meiklejohn and C. P. Bean, Phys. Rev. **102**, 1413 (1956).

[20] V. Skumryev, S. Stoyanov, Y. Zhang, G. Hadjipanayis, D. Givord, and J. Nogués, Nature **423**, 850 (2003).

[21] M. Pellarin, E. Cottancin, J. Lermé, J. L. Vialle, J. P. Wolf, M. Broyer, V. Paillard, V. Dupuis, A. Pérez, J. Pérez, et al., Chem. Phys. Lett. **224**, 338 (1994).

[22] A. Pérez, P. Mélinon, V. Dupuis, P. Jensen, B. Prével, M. Broyer, M. Pellarin, E. Cottancin, J. Lermé, J. L. Vialle, et al., J. Phys. D **30**, 1 (1997).

[23] P. Milani and W. A. de Heer, Rev. Sci. Instrum. **61**, 1835 (1990).

[24] J. L. Rousset, F. J. C. S. Aires, B. R. Sekhar, P. Mélinon, P. Prével, and M. Pellarin, J. Phys. Chem. B **104**, 5430 (2000).

[25] J. L. Rousset, F. J. C. S. Aires, A. Renouprez, P. Mélinon, A. Pérez, M. Pellarin, J. L. Vialle, and M. Broyer, J. Chem. Phys. **102**, 8574 (1995).

[26] M. Gaudry, J. Lerme, E. Cottancin, M. Pellarin, B. Prével, M. Treilleux, Mélinon, and J. L. R. ans M. Broyer, Eur. Phys. J. D **16**, 201 (2001).

[27] L. Favre, S. Stanescu, V. Dupuis, E. Bernstein, T. Epicier, P. Mélinon, and A. Pérez, Appl. Surf. Sci. **226**, 265 (2004).

[28] L. Favre, V. Dupuis, E. Bernstein, S. Stanescu, P. Mélinon, A. Pérez, T. Epicier, J. P. Simon, J. M. Tonnerre, and D. Babonneau, unpublished.

[29] R. van Hardeveld and F. Hartog, Sur. Sci. **15**, 189 (1969).

[30] M. Jamet, V. Dupuis, P. Mélinon, G. Guiraud, A. Pérez, W. Wernsdorfer, A. Traverse, and B. Baguenard, Phys. Rev. B **62**, 493 (2000).

[31] V. Grolier, D. Renard, B. Bartenlian, P. Beauvillain, C. Chappert, C. Dupas, J. Ferr, M. Galtier, E. Kolb, M. Mulloy, et al., Phys. Rev. Lett. **71**, 3023 (1993).

[32] P. Bruno and C. Chappert, Phys. Rev. Lett. **67**, 1602 (1991).

[33] P. Allia, M. Coisson, P. Tiberto, F. Vinai, M. Knobel, M. A. Novak, and W. C. Nunes, Phys. Rev. B **64**, 144420 (2001).

[34] A. Kootte, C. Haas, and R. A. de Groot, J. Phys.: Condens. matter **3**, 1133 (1991).

[35] O. Fruchart, P. O. Jubert, C. Meyer, M. Klaua, J. Barthel, and J. Kirschner, J. Mag. Mag. Mat. **239**, 224 (2002).

[36] W. Grange, I. Galanakis, M. Alouani, M. Maret, J. P. Kappler, and A. Rogalev, Phys. Rev. B **62**, 1157 (2000).

[37] V. Dupuis, M. Jamet, L. Favre, J. Tuaillon-Combes, P. Mélinon, and A. Pérez, J. Vac. Sci. Technol. A **21**, 1519 (2003).

[38] W. Wernsdorfer, E. B. Orozco, K. Hasselbach, A. Benoit, B. Barbara, N. Demoncy, A. Loiseau, H. Pascard, and D. Mailly, Phys. Rev. Lett. **78**, 1791 (1997).

[39] E. C. Stoner and E. P. Wohlfarth, Phil. Trans. Roy. Soc. London **240 A**, 599 (1948).

[40] R. W. Chantrell, A. Lyberatos, M. El-Hilo, and K. O'Grady, J. Appl. Phys. **76**, 6407 (1994).

[41] R. Street and S. D. Brown, J. Appl. Phys. **76**, 6386 (1994).

[42] J. O. Andersson, C. Djurberg, T. Jonsson, P. Svedlindh, and P. Nordblad, Phys. Rev. B **56**, 13983 (1997).

[43] B. Hillebrands and J. R. Dutcher, Phys. Rev. B **47**, 6126 (1993).

[44] R. Morel, A. Brenac, and C. Portemont, J. Appl. Phys. **95**, 3757 (2004).

[45] A. N. Dobrynin, D. N. Ievlev, K. Temst, P. Lievens, J. Margueritat, J. Gonzalo, C. N. Afonso,

S. Q. Zhou, A. Vantomme, E. Piscopiello, et al., Appl. Phys. Lett. **87**, 12501 (2005).

[46] J. I. Hong, T. Leo, D. J. Smith, and A. E. Berkowitz, Phys. Rev. Lett. **96**, 117204 (2006).